Title	Intruder configurations in the ground state of ^{30}Ne
Author(s)	Liu H. N., Lee J., Doornenbal P., Scheit H., Takeuchi Satoshi, Aoi Nori, Li K. A., Matsushita Masafumi, Steppenbeck D., Wang H., Baba Hidetada, Ideguchi Eiji, Kobayashi Nobuyuki, Kondo Yosuke, Lee G., Michimasa Shinichiro, Motobayashi Toru, Poves A., Sakurai Hiroyoshi, Takechi Maya, Togano Yasuhiro, Tostevin J. A., Utsuno Yutaka
Citation	Physics Letters B, 767, p.58-62
Text Version	Publisher's Version
URL	https://jopss.jaea.go.jp/search/servlet/search?5058506
DOI	https://doi.org/10.1016/j.physletb.2017.01.052
Right	

Physics Letters B 767 (2017) 58–62

Contents lists available at ScienceDirect

Physics Letters B

www.elsevier.com/locate/physletb

Intruder configurations in the ground state of ^{30}Ne

H.N. Liu [a,b,*], J. Lee [b,c,*], P. Doornenbal [b], H. Scheit [a,b], S. Takeuchi [b], N. Aoi [b], K.A. Li [a,b], M. Matsushita [b,d], D. Steppenbeck [b], H. Wang [a,b], H. Baba [b], E. Ideguchi [e], N. Kobayashi [f], Y. Kondo [f], G. Lee [f], S. Michimasa [e], T. Motobayashi [b], A. Poves [g], H. Sakurai [b], M. Takechi [b], Y. Togano [b], J.A. Tostevin [h], Y. Utsuno [i]

[a] School of Physics and State Key Laboratory of Nuclear Physics and Technology, Peking University, Beijing 100871, China
[b] RIKEN Nishina Center, 2-1 Hirosawa, Wako, Saitama 351-0198, Japan
[c] Department of Physics, The University of Hong Kong, Pokfulam Road, Hong Kong, China
[d] Department of Physics, Rikkyo University, Toshima, Tokyo 172-8501, Japan
[e] Center for Nuclear Study, University of Tokyo, RIKEN campus, Wako, Saitama 351-0198, Japan
[f] Department of Physics, Tokyo Institute of Technology, Meguro, Tokyo 152-8551, Japan
[g] Departamento de Física Teórica and IFT-UAM/CSIC, Universidad Autónoma de Madrid, 28049 Madrid, Spain
[h] Department of Physics, Faculty of Engineering and Physical Sciences, University of Surrey, Guildford, Surrey GU2 7XH, United Kingdom
[i] Japan Atomic Energy Agency, Tokai, Ibaraki 319-1195, Japan

ARTICLE INFO

Article history:
Received 12 September 2016
Received in revised form 14 January 2017
Accepted 24 January 2017
Available online 27 January 2017
Editor: V. Metag

Keywords:
Intruder configurations
One-neutron knockout reactions
^{12}C(^{30}Ne,^{29}Ne+γ)X

ABSTRACT

We report on the first detailed study of intruder configurations in the ground state of ^{30}Ne by means of the ^{12}C(^{30}Ne,^{29}Ne+γ)X one-neutron knockout reaction at 228 MeV/nucleon. Using a combined analysis of individual parallel momentum distributions and partial cross sections we find: (a) comparable p- and d-wave removal strength to ^{29}Ne final states with excitation energies below 200 keV, and (b) significant p-wave removal strength to the 620 keV state of ^{29}Ne, and (c) no evidence for f-wave intruder strength leading to bound ^{29}Ne final states. The SDPF-U-MIX shell model calculation in the sd–pf model space provides a better overall agreement with the measured energy levels of ^{29}Ne and the fp-intruder amplitudes in ^{30}Ne than the SDPF-M prediction, suggesting that the refinement of the sd–pf cross shell interaction and extension of the model space to include the $2p_{1/2}$ and $1f_{5/2}$ levels are important for understanding the island of inversion.

Exploring the shell evolution from stable to neutron-rich nuclei is a major focus in modern nuclear physics. Systems with exotic combinations of protons and neutrons often exhibit interesting structure behavior, such as quenching of the conventional shell gaps, deformation, and halo structure. The so-called island of inversion [1], a region around neutron-rich $N \sim 20$ nuclei, is a striking example with rapid changes in nuclear structure. The ground states of nuclei in this island are dominated by neutron fp-shell intruder rather than sd-shell normal configurations, owing to the collapse of the $N = 20$ shell closure. In 1975, the first signature of the $N = 20$ shell quenching was found by mass measurements, yielding an increased separation energy for ^{31}Na [2]. Later, low-lying first excited 2^+ states and enhanced $E2$ transition probabilities were observed in ^{32}Mg [3,4] and ^{30}Ne [5,6], showing the presence of large deformation. The driving force behind such unexpected behavior has been investigated with mean-field [7] and shell-model [8–12] approaches. It has been discussed that in neutron-rich nuclei the reduced $T = 0$ tensor forces suppress the separation between the $1d_{3/2}$ and $1f_{7/2}$ orbitals, leading to the intruder dominance by particle–hole excitations across the $N = 20$ shell gap [10].

Over the past two decades, considerable efforts have been expended to explore the exact boundary of the island of inversion and the propagation of the intruder strength along isotopic chains, but details of the structural evolution remain to be fully understood. In the chain of Ne isotopes, experiments [5,6,13–16] confirm the onset of intruder configurations in ^{28}Ne, and placed $^{29-32}$Ne inside the island of inversion. For ^{28}Ne, the p-wave intruder content was found to have a spectroscopic factor (C^2S) of 0.34(2) [13]. Recently, ^{31}Ne has been identified as a deformation driven p-wave halo nucleus with spin parity $3/2^-$ [15]. The cross sections to the ^{30}Ne ground state following the one-neutron ($1n$) removal

* Corresponding authors.
E-mail addresses: hongna@kth.se (H.N. Liu), jleehc@hku.hk (J. Lee).

http://dx.doi.org/10.1016/j.physletb.2017.01.052

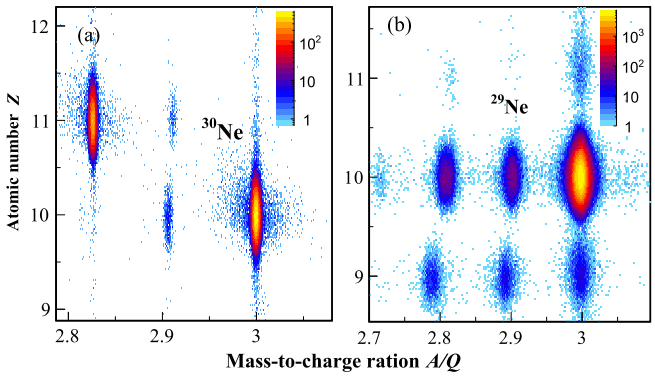

Fig. 1. Particle identification (a) in front of and (b) behind the secondary target.

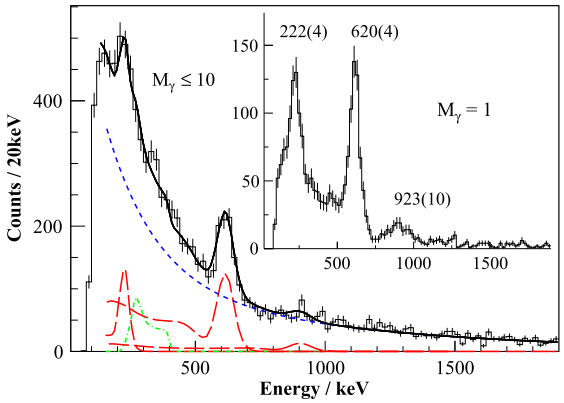

Fig. 2. Doppler-shift corrected γ-ray energy spectrum for the ^{12}C(^{30}Ne,^{29}Ne+γ)X reaction measured using the NaI(Tl) crystals placed at polar angles from 36° to 92° in the ^{29}Ne rest frame with γ-ray multiplicity $M_\gamma \le 10$. The black solid line shows the fit to the spectrum. The red dashed and blue dotted lines represent the simulated response functions for the transitions and two exponentials for the background, respectively. The green dash-dotted line shows the line shape of the "shoulder" around 300 keV which was extracted from the measured γ-ray spectra in coincidence with ^{28}Ne and ^{27}F following 2n and 1p2n removal from ^{30}Ne. The inset shows the spectrum measured using all crystals with γ-ray multiplicity $M_\gamma = 1$. (For interpretation of the references to color in this figure legend, the reader is referred to the web version of this article.)

from ^{31}Ne revealed that the p-wave halo component has a C^2S of $0.32^{+0.21}_{-0.17}$ [15]. These p-wave intruder occupancies observed in ^{28}Ne and ^{31}Ne not only confirm the loss of the $N = 20$ magicity, but also signal the lowering of the $2p_{3/2}$ orbital in these neutron-rich nuclei.

For ^{29}Ne, shell-model calculations predicted a $3/2^+$ ground state with $2p$–$3h$ configurations [9], while the 1n knockout measurement from ^{29}Ne supported an assignment of $3/2^-$ to the ground state with the predominant $3p$–$4h$ configurations [14]. This illustrated the strong intruder strength in neutron-rich Ne isotopes. The isotope ^{30}Ne is expected to consist dominantly of $2p$–$2h$ intruder configurations [8,9,12], sharing a similar nuclear structure with the neighboring $N = 20$ isotone, ^{32}Mg [17]. However, large (∼50%) $4p$–$4h$ intruder amplitudes in the ^{30}Ne ground state were suggested based on the measured cross section in the ^{9}Be(^{32}Mg,^{30}Ne+γ)X two-proton knockout reaction [18]. Such large intruder amplitudes were predicted [19] to help stabilize the heavier fluorine isotopes ^{29,31}F against neutron emission. In the present work, we report on the 1n knockout measurement from ^{30}Ne. The combined analysis of the momentum distributions and partial cross sections for individual bound ^{29}Ne final states allows the spin-parity assignment for the low-lying states of ^{29}Ne as well as a quantitative study of the respective fp-shell intruder amplitudes in the ground state of ^{30}Ne. This new experimental information can provide a stringent test of theory and shed new light on the understanding of the island of inversion.

The experiment was carried out at the Radioactive Isotope Beam Factory (RIBF) at the RIKEN Nishina Center. A primary ^{48}Ca beam with an average intensity of approximately 75 pnA was accelerated up to an energy of 345 MeV/nucleon by the RIBF cyclotrons, and bombarded on a 15-mm-thick rotating Be target. The secondary ^{30}Ne beam, produced by projectile fragmentation, was selected and purified by the BigRIPS fragment separator [20] according to particle magnetic rigidities. The momentum acceptance for the ^{30}Ne beam was ±3%. The beam particles passing through BigRIPS were identified event-by-event with the standard ΔE–$B\rho$-TOF method, in which the energy loss ΔE was measured by an ionization chamber, the magnetic rigidity $B\rho$ was deduced from the measured position at the dispersive focus using parallel plate avalanche counters, and the time-of-flight TOF was obtained via two plastic scintillators. Fig. 1(a) displays the particle-identification plot for the secondary beams, of which 63% is ^{30}Ne.

The secondary beams were incident on a 2.54 g/cm^2 thick C target to induce the 1n knockout reactions. The mid-target energy and the intensity of the ^{30}Ne beam were approximately 228 MeV/nucleon and 300 particles per second, respectively. The DALI2 detector array [21] surrounded the C target to detect the de-excitation γ rays from the secondary reaction residues. DALI2 consisted of 186 NaI(Tl) crystals and covered the polar angles from 18° to 150° in the laboratory frame. For 1 MeV γ rays emitted from nuclei with a velocity of ∼0.6c, a 20% photopeak efficiency and a 10% (FWHM) energy resolution were achieved. After the secondary target, the ^{29}Ne residues were transported to the ZeroDegree spectrometer (ZDS) [20] which was operated in the large acceptance mode. The particle identification of the reaction products used a similar ΔE–$B\rho$-TOF method to that for the secondary beams. A clear separation of the Ne fragments was achieved as shown in Fig. 1(b).

The inclusive cross section for the ^{12}C(^{30}Ne,^{29}Ne)X reaction was measured to be 62(2) mb. The quoted uncertainty arose mainly from the estimation of background contamination (2%) and the acceptance of the ZDS (2%), as well as the selection of particle identification (2%). The background contribution was deduced to be 18(2)% by scaling the measured contamination ratio from the 1n knockout reaction from ^{29}Ne with and without the C target [14], that were performed in the same campaign as our measurement and used the same experimental settings except for the plastic scintillator in front of the secondary target. The scale factor was determined by LISE++ [22] taking into account the difference of cross sections and material thickness. In the analysis, the incident angle and momentum of the ^{30}Ne projectiles were restricted to specific ranges (horizontal angle: −13 to 20 mrad; vertical angle: −15 to 15 mrad; momentum: −2.8 to 2.0%) to ensure that the ^{29}Ne residues were fully accepted by the ZDS. The reaction loss of ^{30}Ne in materials along the beam and residue trajectories, together with the detection efficiency for Ne isotopes in the ZDS was determined by measurements with the unreacted ^{30}Ne.

The Doppler-shift corrected γ-ray energy spectrum for the 1n removal reaction from ^{30}Ne with γ-ray multiplicity $M_\gamma = 1$ is shown in the inset of Fig. 2. Three γ-ray peaks are present at 222(4), 620(4) and 923(10) keV, in good agreement with earlier results [23,24]. No γ–γ coincidences were observed between these transitions, so all the observed peaks are attributed to direct decays to the ground state. Note that because of the detector thresholds, the present measurement had no sensitivity to the possible low-lying states below 200 keV. Due to the Doppler shift, observation of the 222 keV γ-ray peak was only possible for those detectors placed at polar angles from 36° to 92° in the ^{29}Ne rest frame. The proposed level scheme of ^{29}Ne is shown in Fig. 3.

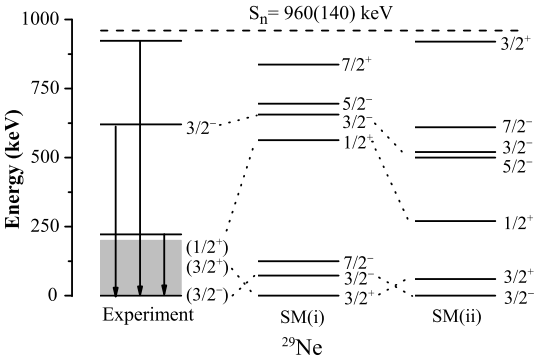

Fig. 3. Comparison of the energy level schemes for ^{29}Ne from the present work and SM calculations. Besides the ground state, a low-lying excited state is inferred to exist below 200 keV, represented by the shaded region. See text for details. The experimental separation energy (S_n) is taken from Refs. [25–27].

It is compared with two sets of shell model (SM) calculations which allow unrestricted mixing of the *sd* and *pf* configurations. Calculation SM(i) uses the SDPF-M effective interaction [9] and the sd–$f_{7/2}p_{3/2}$ model space. Calculation SM(ii) adopts the recently developed SDPF-U-MIX interaction [11,12], and utilizes an extended model space including the $2p_{1/2}$ and $1f_{5/2}$ levels. For ^{29}Ne, both SM calculations predict one or more excited states below the experimental γ detection threshold of 200 keV. The admixture of these low-lying states in the data was examined using the momentum distributions, as will be discussed below.

The γ-ray spectrum in coincidence with the ^{12}C(^{30}Ne, ^{29}Ne)X reaction with γ-ray multiplicities $M_\gamma \leq 10$ was used to determine the partial cross sections. It was confirmed that the γ-ray events with $M_\gamma > 10$ were dominated by background and had negligible contribution to the observed intensities. As shown in Fig. 2, the spectrum was fitted with the GEANT4 simulated response functions for the observed transitions on top of two exponential functions for the background. The validity of the GEANT4 simulation was verified by comparison of the simulated and measured γ-ray spectra with standard sources. The absolute γ-ray detection efficiency from the simulation and source calibration agreed within 3%. It should be noted that a "shoulder" structure around 300 keV, which might originate from the 511 keV and the forward-scattered γ rays, was also included in the fitting function, because this has been observed in the γ-ray spectra in coincidence with ^{28}Ne and ^{27}F following $2n$ and $1p2n$ removal from ^{30}Ne in our measurement. The difference between the results of the fits with and without the "shoulder" component was taken as the systematic error on the cross sections. The measured partial cross sections for all observed states are listed in Table 1. For the 923-keV state, because of its low peak-to-background ratio, a lower limit of the cross section was deduced to be 2.2(4) mb by fitting the spectrum with $M_\gamma = 1$. Assuming the intensity of the 923-keV γ line converges similarly to that of the 620-keV γ line as a function of M_γ, the resulting cross section to the 923-keV state would be 4(1) mb.

The ^{29}Ne parallel momentum distributions in the laboratory frame were derived from the TOF information of the ZDS. The Lorentz transformation was employed with the measured velocity of ^{30}Ne at BigRIPS to eliminate the momentum spread from the incident beam. A momentum resolution of 52 MeV/c (FWHM) was obtained by measuring the unreacted ^{30}Ne ions. The additional momentum spread stemming from the energy loss difference between ^{30}Ne and ^{29}Ne in the reaction target was also considered. As a result, the experimental momentum resolution was deduced to be 59 MeV/c (FWHM).

The momentum distributions for the excited levels were extracted by fitting the γ-ray spectra gated on different regions

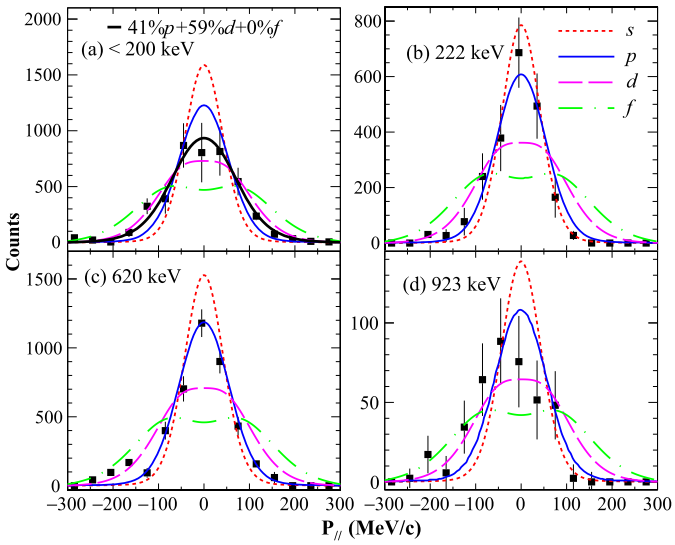

Fig. 4. Individual momentum distributions of the ^{29}Ne residues. Red dotted, blue solid, purple dashed and green dash-dotted lines represent the calculated momentum distributions assuming *s*, *p*, *d*, *f* orbitals occupied by the removed neutron. In (a), the black solid line shows the result of the least-squares fit with the configurations including the *p*, *d* and *f*-wave contents. (For interpretation of the references to color in this figure legend, the reader is referred to the web version of this article.)

of the inclusive momentum. The distribution for states below about 200 keV was reconstructed by subtracting the observed excited-state contributions from the inclusive momentum spectrum. The resulting individual momentum distributions are displayed in Fig. 4. Each distribution is overlaid with several curves that assume removal of the neutron from different single-particle orbitals. These curves represent theoretical distributions, calculated using a reaction model that assumes the sudden and eikonal approximations [28,29], which have been folded with the experimental momentum resolution.

The theoretical inputs in these eikonal model calculations follow the systematic approach detailed in Section III of Ref. [30]. Therefore, the geometries of the complex distorting potentials and the real potentials that bind the removed neutrons are deduced from the ^{29}Ne density and the root mean squared (rms) radii of the active neutron orbitals given by Hartree–Fock (HF) calculations. A Gaussian ^{12}C target density with rms radius of 2.32 fm, consistent with the measured charge radius, and a zero-range effective two-nucleon interaction were assumed. If a (Gaussian) finite-range instead of a zero-range interaction is used in the eikonal model, the calculated cross sections will be increased by ∼5%. Such a small effect will leave the conclusions unchanged. The Woods–Saxon neutron binding potentials in this case have fixed diffuseness (0.7 fm) and spin–orbit strength (6 MeV), while the radius parameters r_0, which were calculated following the procedure and equations in Section III of Ref. [30], were 1.246, 1.133, 1.172 and 1.200 fm for the $1d_{3/2}$, $2s_{1/2}$, $1f_{7/2}$ and $2p_{3/2}$ neutron orbitals, respectively. The depth of each potential was adjusted to reproduce the physical separation energy for the removal reaction to the final state of interest.

The momentum distribution in coincidence with the 620-keV γ rays shown in Fig. 4(c) is well reproduced by the curve with the $l = 1$ assignment. The SM(i) and SM(ii) calculations predict a $3/2^-$ state at 656 and 520 keV, respectively, consistent with the observations. Thereby, the spin parity of the 620-keV excited state is assigned as $3/2^-$. For the 222-keV transition, the derived momentum distribution suggests either $l = 0$ or 1. Compared to the calculated energy level schemes, we tentatively determine $l = 0$

Table 1
Results for the ^{12}C(^{30}Ne,^{29}Ne+γ)X reaction. Measured excitation energies (E_{exp}), determined l values, as well as the experimental partial cross sections (σ_{exp}) and spectroscopic factors (C^2S_{exp}) are listed. The single-particle cross sections (σ_{sp}) are calculated using the eikonal model [28,29]. The predicted excitation energies (E_x), J^π and spectroscopic factors (C^2S_{th}) from the SM(i) [9] and SM(ii) [11,12] calculations are also given.

E_{exp} (keV)	l	σ_{exp} (mb)	σ_{sp} (mb)	C^2S_{exp}	J^π	SM(i)		SM(ii)	
						E_x (keV)	C^2S_{th}	E_x (keV)	C^2S_{th}
<200[a]	(1)	10(5)	35.2	0.25(13)	$3/2^-$	73	0.51	0	0.41
	(2)	14(4)	19.0	0.70(20)	$3/2^+$	0	1.17	60	0.87
			17.0		$7/2^-$	125	1.78	610	1.51
		$\sigma_{<200\,keV} = 24(4)$							
222	(0, 1)	12(3)	30.5	0.36(8)	$1/2^+$	563	0.28	270	0.67
620	1	24(2)	32.3	0.66(7)	$3/2^-$	656	0.13	520	0.30
923	(1, 2, 3)	>2.2(4)[b]							
					$5/2^-$	695	–	500	0.05
					$3/2^+$	1365	0.09	920	0.10
		$\sigma_{inc.} = 62(2)$							

[a] The ground state and low-lying excited state below 200 keV cannot be resolved because of the detector thresholds.
[b] The cross section would be 4(1) mb, if we assume that the intensity of 923-keV γ line converges similarly to that of 620-keV as a function of M_γ. See text for details.

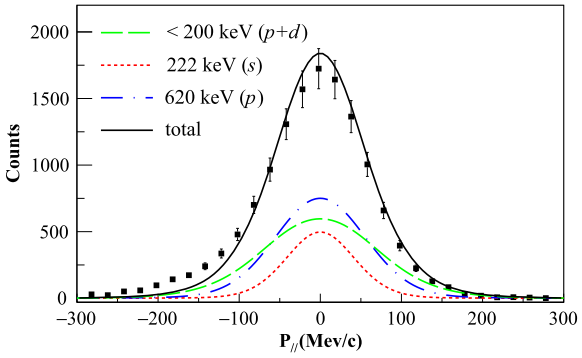

Fig. 5. Inclusive parallel momentum distribution of ^{29}Ne knockout residues. The black solid line shows the theoretical inclusive momentum profile with the experimental orbital assignments for the observed states. The individual contributions from different final states are normalized based on the measured cross sections.

for the removed neutron and assign ($1/2^+$) for the 222-keV state. Although the measured distribution for the 923-keV transition carries very large uncertainty, due to the low statistics, it is clear that its l-value is greater than 0 and less than or equal to 3.

The momentum distribution for states below about 200 keV is shown in Fig. 4(a). It suggests a superposition of different l-values, the distribution being poorly described by any single theoretical curve. This situation is consistent with the SM calculations, which predict either two ($3/2^-$ and $3/2^+$) or three ($3/2^+$, $3/2^-$ and $7/2^-$) states below 200 keV. To extract a best description of the data, we performed a least-squares fit with a linear combination of the p, d and f-wave configurations. The thick black solid line represents this best fit to the data that consists of 41^{+19}_{-19}% p-, 59^{+14}_{-14}% d- and negligible (0^{+1}%) f-wave strength.

The orbital angular momentum assignments for the observed states were further verified using the inclusive momentum distribution. The width of the measured inclusive momentum distribution was deduced (by Gaussian fitting) to be 138 (5) MeV/c (FWHM). As shown in Fig. 5, the eikonal model calculations with the proposed orbital assignments agree well with the data with a calculated width of 137 MeV/c (FWHM); whereas the width of the theoretical distribution assuming pure $l = 1$ or $l = 2$ configurations for states below 200 keV would be 128 or 147 MeV/c (FWHM). This strongly supports the proposed admixture of these two l-values from the individual momentum analysis. The contributions from each final state, normalized by the measured cross sections, are also shown in Fig. 5. It is apparent that the population of states involving neutron removal from low l-orbitals is dominant and is consistent with a small f-wave contribution.

We now elucidate the spin-parity assignment for the ground state of ^{29}Ne. In our study, we find almost equal amounts of ^{29}Ne with $l = 1$ and $l = 2$ in the extracted momentum distribution for bound final states with excitation energies below 200 keV, suggesting that ^{29}Ne has a ground state of $3/2^-$ or $3/2^+$. In the β-decay of ^{29}Ne, the large branching ratio observed to the $5/2^+$ ground state of ^{29}Na was indicative of an assignment of $3/2^+$ [31,32], but the 1n removal measurement from ^{29}Ne lent a strong support to a $3/2^-$ ground state of ^{29}Ne [14]. Taken together with the measured enhanced interaction cross section of ^{29}Ne with respect to ^{28}Ne, which indicated low-l valence neutron configurations [33], the $3/2^-$ assignment was adopted for the ground state of ^{29}Ne in the current analysis. The resulting picture that ^{29}Ne has a $3/2^-$ ground state with a very low-lying $3/2^+$ excited state (without the low-lying $7/2^-$ state) poses a stringent test for the adopted two SM analyses and is in agreement with the SM(ii) calculation, as illustrated in Fig. 3.

Further characterization of the observed states is obtained from the spectroscopic strengths of neutrons in fp intruder orbitals. The required single-particle cross sections (σ_{sp}) are computed in the eikonal model using the same S-matrices and bound state inputs as are used to calculate the momentum distributions. The ratio of the measured partial cross section to the calculated σ_{sp} gives the associated C^2S_{exp}.

As shown in Table 1, the p-wave C^2S_{exp} for the states below 200 keV and the 620-keV state are 0.25(13) and 0.66(7), respectively. We note that if $3/2^-$ is not the ground state but a low-lying excited state of ^{29}Ne, the deduced C^2S_{exp} for states below 200 keV will change by less than 3% because of the small excitation-energy difference. The total p-wave strength deduced for the ground state of ^{30}Ne is thus 0.9(1), much larger than that observed [0.34(2)] for ^{28}Ne from the 1n removal [13]. This enhanced probability of neutrons residing in the p-intruder orbital shows the lowering of the $2p_{3/2}$ orbital and provides a direct evidence for the SIMULTANEOUS breakdown of the $N = 20$ and $N = 28$ shell gap. To further test the shell-model interactions in this region, we compare these p-wave C^2S_{exp} with the predictions from SM(i) and SM(ii). It is found that the SM(i) calculation overestimates the C^2S for the states below 200 keV by a factor of 2, but underestimates that for the 620 keV state by a factor of 5, leading to an inadequate description for the inclusive p-wave C^2S_{exp}. The larger inclusive p-wave intruder component than the SM(i) prediction was also reported for ^{33}Mg based on the measured inclusive parallel momentum distribution from the 1n removal reaction [34]. On the other

hand, our work shows that SM(ii) shifts the spectroscopic strength from the first to the second $3/2^-$ state of ^{29}Ne and enhances the C^2S for the 620 keV state compared to SM(i), resulting in a better agreement with both the partial and total p-wave $C^2S_{\rm exp}$.

For the f-wave intruder component, a negligible spectroscopic strength is found in the ^{12}C(^{30}Ne,^{29}Ne)X reaction. However, SM(i) predicts that the $7/2^-$ state in ^{29}Ne lies at 125 keV and carries a large $C^2S_{\rm th}$ of 1.78. It is interesting that the f-wave intruder content in ^{32}Mg, the $N=20$ isotone next to ^{30}Ne, was found to have a $C^2S_{\rm exp}$ of 1.19(36), larger than the p-wave $C^2S_{\rm exp}$ [0.59(11)] [17]. Meanwhile, all evidence to date suggests that ^{30}Ne is well deformed and has a total neutron fp-intruder occupancy $n(fp)\geq 2$ [5,6,18]. In this work, however, the deduced neutron p-shell occupancy is 0.9(1), much smaller than the expected $n(fp)\geq 2$. Therefore, it is likely that significant f-wave intruder content exists in ^{30}Ne. The absence of the f-wave intruder strength in the present measurement is probably due to the $7/2^-$ state in ^{29}Ne lying above the neutron separation energy $S_n = 960(140)$ keV [25–27]. Such a scenario has been observed for ^{27}Ne via the ^{26}Ne$(d,p)^{27}$Ne reaction [35]. This reaction proposed that the $7/2^-$ intruder state in ^{27}Ne was unbound and located at an excitation energy of 1.74(9) MeV [35], ∼1.5 MeV higher than the SM(i) prediction. When extending the model space from sd–$f_{7/2}p_{3/2}$ to sd–pf and exploiting the recently developed SDPF-U-MIX interaction, the predicted excitation energy of the $7/2^-$ state of ^{29}Ne in the SM(ii) calculation is pushed to 610 keV. While ∼0.5 MeV higher than the SM(i) prediction, the predicted energy is still below S_n.

It is worth noting that the SM(i) and SM(ii) calculations predict very similar excitation energies of the first 2^+ state for all neutron-rich Ne isotopes (from ^{26}Ne to ^{32}Ne) [12,16], and both agree well with the experimental data. The sensitivity to the different SM interactions revealed by the measured energy level scheme of ^{29}Ne and the fp-intruder amplitudes in ^{30}Ne in the current work is thus very instructive. The better overall agreement between the SM(ii) prediction and the observations suggests that the refinement of the sd–pf cross shell interaction and the extension of the model space to include the $2p_{1/2}$ and $1f_{5/2}$ levels are important for a better understanding of the island of inversion.

In summary, the ^{12}C(^{30}Ne,^{29}Ne+γ)X single-neutron knockout reaction at 228 MeV/nucleon was performed at the RIBF, providing the first quantitative information on intruder configurations in the ground state of ^{30}Ne. Using the combined analysis of individual parallel momentum distributions and partial cross sections, we find (a) comparable p- and d-wave removal strength to ^{29}Ne final states with excitation energies below 200 keV, and (b) significant p-wave removal strength to the 620 keV state of ^{29}Ne, and (c) no evidence for f-wave intruder strength leading to bound ^{29}Ne final states. The total p-wave intruder strength observed in this work is 0.9(1), providing direct experimental evidence for the breakdown of the $N=20$ and $N=28$ shell gap, while our non-observation of f-wave strength supports that the $7/2^-$ state in ^{29}Ne is unbound. Two shell model calculations have been used to compute the structure of ^{29}Ne and ^{30}Ne. Compared to the SDPF-M calculation in the sd–$f_{7/2}p_{3/2}$ model space, the SDPF-U-MIX calculation in the sd–pf model space offers an overall improvement for the description of the experimental energy levels of ^{29}Ne and the fp-intruder amplitudes in ^{30}Ne. This comparison demonstrates the sensitivity of knockout reactions to the shell-model interactions in this region, and suggests that the refinement of the sd–pf cross shell interaction and extending the model space to include the $2p_{1/2}$ and $1f_{5/2}$ levels are crucial for a comprehensive understanding of the island of inversion.

Acknowledgements

We thank the RIBF accelerator staff for their work in the primary beam delivery and the BigRIPS team for preparing the secondary beams. We thank Y.L. Ye, Z.H. Li and I. Hamamoto for their fruitful discussions. J.A. Tostevin acknowledges the support of the Science and Technology Facilities Council (UK) grant ST/L005743. A. Poves acknowledges the support of MINECO (Spain) grant FPA2014-57196 and Programme “Centros de Excelencia Severo Ochoa” SEV-2012-0249.

References

[1] E.K. Warburton, et al., Phys. Rev. C 41 (1990) 1147.
[2] C. Thibault, et al., Phys. Rev. C 12 (1975) 644.
[3] B.V. Pritychenko, et al., Phys. Rev. C 19 (1979) 164.
[4] T. Motobayashi, et al., Phys. Lett. B 346 (1995) 9.
[5] Y. Yanagisawa, et al., Phys. Lett. B 566 (2003) 84.
[6] P. Doornenbal, et al., Phys. Rev. C 93 (2016) 044306.
[7] X. Campi, et al., Nucl. Phys. A 251 (1975) 193.
[8] E. Caurier, et al., Nucl. Phys. A 693 (2001) 374.
[9] Y. Utsuno, et al., Phys. Rev. C 60 (1999) 054315.
[10] T. Otsuka, et al., Phys. Rev. Lett. 87 (2001) 082502.
[11] A. Poves, et al., Phys. Scr. T150 (2012) 014030.
[12] E. Caurier, et al., Phys. Rev. C 90 (2014) 14302.
[13] J.R. Terry, et al., Phys. Lett. B 640 (2006) 86.
[14] N. Kobayashi, et al., Phys. Rev. C 93 (2016) 014613.
[15] N. Nakamura, et al., Phys. Rev. Lett. 112 (2014) 142501.
[16] P. Doornenbal, et al., Phys. Rev. Lett. 103 (2009) 032501.
[17] J.R. Terry, et al., Phys. Rev. C 77 (2008) 014316.
[18] P. Fallon, et al., Phys. Rev. C 81 (2010) 041302.
[19] Y. Utsuno, et al., Phys. Rev. C 64 (2001) 011301(R).
[20] T. Kubo, et al., Prog. Theor. Exp. Phys. 2012 (2012) 03C003.
[21] S. Takeuchi, et al., Nucl. Instrum. Methods Phys. Res., Sect. A 763 (2014) 596.
[22] O.B. Tarasov, D. Bazin, Nucl. Instrum. Methods Phys. Res., Sect. B 266 (2008) 4657.
[23] M. Belleguic, et al., Phys. Rev. C 72 (2005) 054316.
[24] E. Rodriguez-Vieitez, Ph.D Thesis, University of California, Berkeley, California, 2007.
[25] G. Audi, et al., Chin. Phys. C 36 (2012) 1287.
[26] M. Wang, et al., Chin. Phys. C 36 (2012) 1603.
[27] B. Jurado, et al., Phys. Lett. B 649 (2007) 43.
[28] J.A. Tostevin, J. Phys. G: Nucl. Part. Phys. 25 (1999) 735.
[29] P.G. Hansen, J.A. Tostevin, Annu. Rev. Nucl. Part. Sci. 53 (2003) 221.
[30] A. Gade, et al., Phys. Rev. C 77 (2008) 044306.
[31] V. Tripathi, et al., Phys. Rev. Lett. 94 (2005) 162501.
[32] J. Lee, et al., Prog. Theor. Exp. Phys. 2016 (2016) 083D01.
[33] M. Takechi, et al., Phys. Lett. B 707 (2012) 357.
[34] R. Kanungo, et al., Phys. Lett. B 685 (2010) 253.
[35] S.M. Brown, et al., Phys. Rev. C 85 (2012) 011302(R).